Focusing of Internal Tides by Near-inertial Waves

Y. Cuypers[1], P. Bouruet-Aubertot[1], J. Vialard[1], M.J. McPhaden[2]

1. LOCEAN-IPSL, Sorbonne Univ. (UPMC, Univ Paris 06)-CNRS-IRD-MNHN, Paris, France

2. Pacific Marine Environment Laboratory, NOAA, Seattle, USA

Submitted to *Geophysical Research Letters*

Submitted, February 20th 2016

Revised version, January 12th 2017

Corresponding author address:

Y. Cuypers

LOCEAN – Case 100, Université Pierre et Marie Curie

4, Place Jussieu

75252 Paris Cedex 05

France

E-mail: yannis.cuypers@locean-ipsl.upmc.fr

Abstract

The refraction of internal waves by lower-frequency near-inertial waves has been predicted theoretically, but never observed before. Here, we report observations of semi-diurnal internal tides generated by the rough topography of the Central Indian Ridge, in the presence of a strong, lower-frequency near-inertial wave field generated by a tropical storm. The semi-diurnal internal tide energy is trapped within upward-propagating bands with a periodicity close to the inertial period. A ray-tracing model suggests that this trapping results from the internal tide refraction by the shear associated with near-inertial waves. This yields a strong increase of the internal tide energy and shear in space-time regions where the background flow focuses the rays, leading to the formation of caustics. This mechanism may increase vertical mixing generated by baroclinic tides in the vicinity of mid-ocean ridges in tropical regions.

1 Introduction

Internal tides are believed to be a key source of the vertical mixing necessary to sustain the global overturning circulation (Wunsch and Ferrari, 2004). Internal tides develop as the result of the interaction of barotropic tides with bottom ocean topography. Abyssal generation of internal tides from mid-ocean ridges represents about 25% of the total power dissipated by barotropic tides (Egbert and Ray, 2001). Mid-ocean ridges are characterized by their rough small-scale topography, and internal tides generated there are associated with relatively small horizontal and vertical wavelengths (St. Laurent and Garrett, 2002, St. Laurent and Nash, 2004). It is estimated that ~30% of internal tide energy generated at mid-ocean ridges is dissipated locally near the bottom (Polzin et al., 1997) while the remaining ~70% propagates away from the source and contributes to background mixing away from the oceanic bottom and source region (St. Laurent and Garrett, 2002).

The dissipation mechanism for the ~70% of internal tide energy radiated away from the bottom remains unclear. Recent studies have shown that the scattering of low vertical mode internal tides by the sub-inertial mesoscale field (Rainville and Pinkel 2006, Chavanne et al., 2010, Zaron and Egbert, 2014, Ponte and Klein, 2015) or topographic features (Kelly et al., 2013), and the subsequent generation of higher vertical modes, is a possible dissipation mechanism. In parallel, theoretical and idealized numerical studies suggest that short horizontal and vertical wavelength internal waves with upward energy propagation, including internal tides, can be strongly affected by the ubiquitous lower-frequency near-inertial waves with upward phase propagation such as those generated by storms (Broutman and Young, 1986, Broutman, 1986, Broutman et al., 1997, Vanderhoff et al., 2008). The varying background shear associated with lower-frequency (near-inertial) waves create waveguides that can focus the higher frequency internal waves into regions where the high resulting shear can lead to high energy dissipation (Broutman 1986). The time-dependence of the inertial wave field is crucial in this mechanism, which is thus fundamentally different from the classical critical layer mechanism (Olbers, 1981). This process could in particular be efficient close to the surface, where strong near-inertial motions occur in response to changing winds. The formation of caustics (i.e. space-time regions where a time varying background flow focuses the internal tide energy) has to our knowledge not yet been observed from in-situ data.

About 100 GW of M2 barotropic tidal energy is converted to baroclinic tides by the rough small scale topography on the Central Indian Ocean Ridge (Egbert and Ray, 2001, Nycander, 2005, Melet et al., 2013), making this region a hotspot for turbulent vertical mixing in the global ocean (Whalen et al., 2012). Tropical storms also form in this region, such as the developing Dora cyclone observed during the 2007 Cirene cruise (Vialard et al., 2009). The generation of downward propagating near-inertial waves by the Dora cyclone was observed and described by Cuypers et al. (2013). The Cirene cruise area is thus a region where there are both strong internal tides and wind-generated inertial waves, which could lead to the formation of caustics. Internal tides generated in this region have also not yet been described from in-situ measurements. The goal of this article is to characterize internal tides generated at the Central Indian Ocean Ridge and their potential modulation by near-inertial internal waves.

2 Data and methods

The Cirene cruise and observations are described in detail in Vialard et al. (2009). The cruise was conducted in two legs, each involving a 10-12 days station near 8°S, 67°30'E (January 14-26 and February 4-15). The Dora tropical Storm formed in the interval between the two legs. In this study we use conductivity temperature depth (CTD) casts performed roughly every 20 minutes down to 500 m and CTD and Lowered-Acoustic Doppler Current Profiler (L-ADCP) profiles down to 1000 m roughly every 6 hours. Post-processed CTD data have 1 m vertical resolution and post-processed L-ADCP data provide horizontal currents at 8 m vertical resolution.

In order to get a more comprehensive picture of semi-diurnal (hereafter, SD) internal tide generation and propagation in the Cirene region, we used the Gerkema (2002) 2D linear internal tide generation model. The model requires the prescription of the barotropic tidal flux, the topographic section in the model plane and the buoyancy frequency profile $N(z)$. Barotropic fluxes were specified from the TPXO.7.1 global tidal model (Egbert and Erofeeva, 2002). We considered the two main SD tidal components (M2, S2), which contribute to 98.5% of the semi diurnal variance. The model plane was chosen along the SD ellipses (135° from parallels), which are very eccentric, almost exactly aligned along the strongest topographic gradient with weaker topographic fluctuations in the perpendicular direction (Fig. 1a). This configuration makes the 2D assumption reasonable. The model domain spans 800 km centered on the Cirene station, with 400 m horizontal resolution, and 60 degrees of freedom in the vertical. The topographic profile is a linear interpolation from the 1 to 12 km resolution Smith and Sandwell (1997) bathymetry (V18.1). The stratification profile $N(z)$ is obtained from the cruise-average of CTD profiles down to 1000 m, completed with climatological values derived from the World Ocean Atlas 2013 (Locarnini et al., 2013, Zweng et al., 2013) down to the bottom.

The interaction between the SD internal tide and Near-inertial internal Waves (NIWs hereafter) is investigated using an Eikonal equation as in Broutman (1986). Eikonal equations describe the evolution of a test internal wave, in our case the internal tide, in a slowly varying medium in time and/or space. The wave is described in terms of density fluctuations $\rho' = a\exp(i\theta)$ where $\mathbf{k} = (k,0,m) = \nabla_{\mathbf{x}}\theta$ is the wavenumber and $\omega_i = \partial_t\theta$ the intrinsic frequency. The background medium is defined from the velocity **U** and stratification N, **k** and ω_i are related through the internal waves dispersion relationship:

$$\omega_i^{\,2} = \frac{N^2k^2 + f^2m^2}{k^2 + m^2} \qquad (1)$$

Since the medium is moving with the velocity **U,** there is a Doppler shift between ω_i and the ω_0 frequency observed from a fixed point: $\omega_0 = \mathbf{U}.\mathbf{k} + \omega_i$. We also assume that there are no background and wave energy density variations along the horizontal. The Eikonal equations governing the ray energy propagation read:

$$\mathbf{c_g} = \frac{d\mathbf{x}}{dt} = \nabla_{\mathbf{k}}\omega_0 \qquad (2)$$

$$\frac{dm}{dt} = -\frac{\partial\omega_0}{\partial z} = -\frac{k^2NN_z}{(k^2+m^2)\omega_i} - kU_z \qquad (3)$$

$$\frac{\partial A}{\partial t} + \nabla_{\mathbf{x}}\left[\mathbf{c_g}A\right] = 0 \qquad (4)$$

Equations (2) and (3) yield the ray trajectory and the evolution of the vertical wavenumber along the ray. The third equation expresses the conservation of the wave action $A = E/\omega_i$ with the energy density E, related to density fluctuations amplitude a through

$E = 2PE\left[1+\left(\frac{fm}{Nk}\right)^2\right]$ and $PE = \frac{1}{4}\frac{g^2 a^2}{\rho_0 N^2}$ the Potential Energy density. The set of equations is integrated numerically using a 4th order Runge-Kutta scheme with partial steps. We integrate the volume element of a ray tube $V = 1/A$ rather than the wave action equation, as in Hayes (1970). This quantity vanishes at caustics (ray convergence points) rather than displaying a singular behavior. The initial conditions for the internal tide and the NIW are based on the observations (supplementary material). We will discuss the validity of this ray-tracing approach in section 4.

3 Results

3.1 Near-inertial waves

As previously described in Cuypers et al. (2013), the Dora tropical storm passed close to the Cirene area between the two legs and generated a strong NIW response during the second leg. This is reflected in the Kinetic Energy (KE) spectrum of 0-500 m averaged L-ADCP velocities, which displays a clear near-inertial (1.2f +/-0.15f) peak during the second leg, but not during the first (Fig.1b). The PE spectrum also displays a near-inertial peak during the second leg, with much less energy than on the KE spectrum due to the weak PE/KE ratio of NIWs.

NIWs are characterized by upward phase (and downward energy) propagation. Their velocity fluctuations can hence be isolated by extracting upward phase propagating signals as in Cuypers et al. (2013) (Fig. 2ab). This confirms that the NIW signal is much stronger during the second leg, and that the downward energy propagation can be tracked using the WKB method (dashed lines in Fig. 2b, see Cuypers et al. 2013 for details).

3.2 Strong semi-diurnal tide signal

Cirene data also indicate a clear tidal signal during both legs. The L-ADCP sampling frequency (~ 4 day^{-1}) is not sufficient to resolve the SD internal tide peak. The frequent CTD measurements (~ 3 $hour^{-1}$) however allow estimating the Potential Energy (PE) spectrum over a wider frequency range. The PE spectrum displays a diurnal peak and the dominant peak is associated with the SD internal tide for both legs. The frequency resolution is however not sufficient to distinguish the close M2 and S2 periods.

The 2D internal tide model (ITide model in the following) allows to better understanding the origin of the relatively strong SD tidal signal at the Cirene site. It displays a complex array of narrow SD internal tide beams generated by the rough topography (Fig. 3a). The Cirene station (x=0 km) is exactly co-located with an energy near-surface local maximum, corresponding to the convergence and surface reflection of two internal tidal beams generated from two neighboring ridges at x=65 km and x=-60 km. The vertically-integrated energy flux (Fig. 3b) indeed displays two strong gradients near these positions, implying strong internal tide generation there. The red lines on Fig. 3a indicate the rays emanating from those ridges, computed using the WKB theory in the simple case of a stationary beam with no background velocity, as in the ITide model simulation. In this case the ray slope is simply defined by $dz/dx = \pm\left[\left(\omega^2 - f^2\right)/\left(N(z)^2 - \omega^2\right)\right]^{1/2}$. The ray trajectory closely matches the energy beam of the ITide model, even in the pycnocline where the WKB hypothesis (slow variation of stratification) in principle breaks down. This suggests that the eikonal equations (2-4) can be used to study internal semi diurnal tide packets trajectories.

The ITide model can be validated from Fig. 3d and e, which compare the time-averaged SD PE in the model and Cirene data for both legs. The model is linear with uniform background, and thus generates very focused beams associated with strong PE spatial gradients. Beams are likely less focused in reality because of dissipation and internal reflections (Gerkema and Van Haren, 2012) and we hence compare the model average within 5 km (roughly half the beam width) of the Cirene station to Cirene observations. Observed and simulated average PE profiles match reasonably well for both legs. There is a reasonable match between the ITide model and the data which give some confidence that the internal tides are indeed generated from the nearby ridges. We will show in the next section how the NIW and time mean background currents during leg2 strongly alter the internal tide propagation.

3.3 Focusing of internal tides by near-inertial internal waves

In order to characterize SD tide spatial scales, the density field was also separated into ρ'_{up} with upward and ρ'_{dn} with downward phase propagation. The SD internal tide phase as a function of depth $\varphi(z)$ was obtained from demodulation of ρ'_{dn}, over the first half of leg2 (Feb 4-Feb 10), before the tide could significantly interact with the NIW packet. The nearly linear shape of $\varphi(z)$ between 250 m and 500 m (not shown) implies an initial vertical wavenumber $m_0 = 8.06\times10^{-3}$ rad m^{-1} with a $[8.03\times10^{-3}$ - $8.08\times10^{-3}]$ 95% confidence interval. Applying the dispersion relationship (1) with the average N value in this depth range leads to a horizontal wavelength of ~23 km. The same procedure applied to the first leg (when there was hardly any NIW signal) yields similar numbers: $m_0 = 9.84\times10^{-3}$ [9.82×10^{3}- 9.86×10^{-3}] rad m^{-1} and ~18 km. The internal tide horizontal wavelength is a bit larger in the ITide model, where the horizontal wavenumber spectrum of buoyancy fluctuations (not shown) displays a broad peak at ~ 30 km. This may result from the strong presence of small-scale abyssal hills in the Central Indian Ridge which can enrich the high wavenumber modes (Melet et al., 2013) but which are smoothed in the Smith and Sandwell (1997) bathymetry used in the ITide model.

We have band pass filtered ρ'_{dn} using an elliptical filter (Park, 1987) in the [$0.8\omega_{SD}$-

$1.2\omega_{SD}$] frequency band in order to isolate the SD tide signal. The PE for an internal tide with upward energy propagation (downward phase propagation) is $PE_{dn} = \frac{1}{2}\frac{g^2}{\rho_0 N^2}\left\langle \rho'^{\,2}_{dn} \right\rangle_{T_{SD}}$ and is represented in Fig. 2d and 2e for leg1 and leg2 respectively. During the first leg, the SD PE roughly follows the spring / neap cycle of the barotropic tide (displayed in Fig. 2g), with most SD tide signal between the 19^{th} and 25^{th} of January.

There is also a clear modulation of the SD tide by the spring/neap cycle during the second leg, with much less energy after the 10^{th} of February (Fig. 2e and red curve on 2h). The most striking feature is however a very clear modulation of the SD energy with a period close to the NIW period down to 350 m. This modulation propagates upward (Fig. 2e) and the similarity with the NIW current variations (Fig. 2b) is striking.

The observed SD energy maxima vertical propagation velocity (roughly 1×10^{-3} m s^{-1} between 150 m and 300 m) is not consistent with the group velocity of the internal tide. This group velocity should indeed be about one order of magnitude larger, considering the horizontal wavelength of 20 km and mean value of N for this depth range. There is a clear scale separation between the NIW and SD internal tide, not only in frequency (SD~7f), but also in horizontal wavenumber. The NIW is characterized by a ~ 250-300 km horizontal wavelength (Cuypers et al., 2013), about one order of magnitude larger than the internal tide. In the vertical, this scale separation is not as clear, with a ratio of the internal tide to the NIW vertical wavelength of order one (see supplementary material). Previous studies have however used the WKB hypothesis successfully in such a marginal cases (e.g. Rainville and Pinkel, (2006), Chavanne, (2010) or Sheen et al (2015)). Sartelet (2003) has more specifically shown a very good match between a high resolution numerical model and the eikonal equation in a very similar context to the one we study in the present paper. She concludes that “ray theory performs remarkably well even when the scale separation between the background wave and the gravity wave breaks down completely both in the vertical and time”. We have therefore used equations (2) to (4) confidently to model the propagation of an internal tide ray emanating from the eastern ridge in Fig. 3 and propagating westward. The rays emanating from the western ridge do not cross the Cirene station when background NIW and time-mean currents are considered and are therefore not discussed in the following. We only consider the mean observed background velocity for the first leg (Fig. 2g). For the second leg, we consider the mean observed background velocity (Fig. 2h) or alternatively both the mean current and the NIW velocity fluctuations (Fig. 2f). The initial conditions and NIW velocity fluctuations for the second leg (Fig. 2c) were constructed to mimic observations (compare Fig. 2b and 2c): details are given as supplementary material.

For the first leg simulation, the ray trajectories are invariant, the slope of the rays decreases within the pycnocline while the tidal PE increases (Fig. 2g). The overall observed increase in amplitude of the SD tide associated with the spring-neap cycle toward the end of the first leg (Fig. 2d) is reproduced with a lag of ~1 to 2 days relative to barotropic forcing, consistent with the propagation time of SD tides from the generation sites to the Cirene station. Observations however display shorter time scale fluctuations, possibly associated with the weak NIW activity during the first leg, not considered in our calculations. These fluctuations could also result from interactions with remotely generated internal tides (Kelly and Nash, 2010).

The PE distribution obtained when only considering the second leg average current in the Eikonal model is similar to that of the first leg, just showing a spring-neap cycle (Fig. 2h), and very different from the observed modulation of SD tides at near-inertial frequencies (Fig. 2e). Including the refraction by NIWs gives a picture in much better qualitative agreement with observations, with upward propagating bands of SD PE. The second leg ray trajectories are shown on Fig. 2c, with the prescribed NIW field as a background. SD tide packets have an initial group velocity c_{gz}, which exceeds the NIW phase speed C_{NIW} when they penetrate the NIW packet, as revealed by the slope of the rays relative to the slope of the NIW phase. Broutman et al. (1997) classified the different interactions between an inertial wave and a shorter wave as a function of the $r = c_{gz} / C_{NIW}$ ratio before the interaction. For $r >> 1$ (as in our case, for which $r \cong 10$), a strong convergence of wave action is expected, leading to a strong increase in the amplitude of the short waves. The internal tide rays form a caustic when they approach NIW shear maxima. Positive NIW shear indeed induces a strong refraction, characterized by a strong vertical wavenumber modulus increase (Eq. 3), and a group velocity (e.g. ray slope) that becomes lower than C_{NIW}. The region of strong refraction propagates upward along with the region of strongest NIW shear. The time variations of the ray slopes lead to the formation of caustics, defined as the envelope of space-time regions where the rays converge. After the caustic, the rays interact with the NIW field a second time in the upper part of the water column (above 150 m depth). The negative NIW shear induces a vertical group velocity increase and generates a second caustic. Following Broutman (1986), we can define caustics as points where $c_{gz} = C_{NIW}$, i.e. with a zero internal tide group velocity in a frame of reference moving at the NIW phase speed. In Fig. 2c these caustics are plotted as continuous magenta curves, choosing the arbitrary numerical criterion that c_{gz} and C_{NIW} differ by less than 1%.

The refraction and focusing of the internal tide by the NIW generates an alternation of shadowed regions with no tidal energy and higher energy bands (Fig. 2f), with the NIW period. The strongest PE increase is observed when rays approach caustics. As discussed by Broutman (1986) and Vanderhoff (2008), the assumption of a slowly-varying medium breaks down near caustics, yielding unrealistically high wave amplitude. Broutman (1986) suggests a corrected maximum amplitude at the caustic, assuming that the wave envelope is given by an

Airy-function. Fig. 2i displays the PE computed using Broutman's correction along a selected ray (whose trajectory in (z,t) and (x,z) plane is represented as a thick black dashed curve in Fig. 2f and 3f respectively). The ray experiences strong refraction and PE increase at the two caustics. We also show the internal tide Richardson number $Ri = N^2 / {u_z}^2 = k^{-2}(2/\rho_0)^{-1/2}\omega_i(1 - f^2/\omega_i^2)A^{-1}$, whose values below ¼ characterize potential shear instability. The strong refraction of the first ray yields a more than an order of magnitude decrease of the Ri values, relative to when refraction by NIWs is not considered. While Ri (~1) remains above the critical value, this strong localized increase of the shear will combine with other background shear variations, potentially leading to "bursts" of intense vertical mixing. This underlines the potential consequences of this ray-focusing mechanism on vertical mixing in the upper ocean.

4 Discussion

The Cirene data is characterized by strong NIW activity during the second leg, after the passage of tropical storm Dora, with scales of ~3 days and ~300 km (Cuypers et al. 2013). The data also reveals a strong semi-diurnal internal tide activity of ~20 km horizontal scale, generated by the interaction of barotropic tides with two nearby ridges. Here, we report the first observations of SD internal tide amplitude modulation by the larger-scale, lower-frequency NIW fluctuations. Ray tracing using the Eikonal equation suggests that the NIW velocity field can strongly focus the internal tide energy along caustics and induce large space and time fluctuations of the internal tide amplitude and wavenumber at NIW spatio-temporal scales, as first theoretically described by Broutman et al. (1997) and Vanderhoff et al. (2008). Most of the internal tide rays are strongly refracted by the NIW shear, giving rise to two caustic points in the upper 150 m. The strong decrease of the Richardson number at the caustic points is potentially conducive to “bursts” of vertical mixing there.

The ray tracing approach in this paper neglects potentially important effects such as ray scattering by stratification or currents horizontal heterogeneities, the three-dimensional character of the SD energy radiation associated with real bathymetry, and possible nonlinear effects such as wave breaking or energy leaks to the diurnal frequency by PSI (Sun and Pinkel, 2013) which can lead to the degradation of the I-Tide beam in the pycnocline (Gayen and Sakar, 2013). It is hence not surprising that the agreement between Figs. 2e and f is only qualitative. Yet the ray tracing captures the observed SD energy trapping along bands that display vertical propagation at a speed close to the NIW phase speed, while those bands disappear when the refraction mechanism is neglected (Fig. 2h). We also examined alternative mechanisms for semi-diurnal tide modulation at near-inertial frequencies in the supplementary information. NIW-induced stratification variations are too weak to explain the observed variations. Considering beams of finite width instead infinite width as presented here yields advection of the rays that can induce SD tide amplitude variation at a given point, due to the varying distance between the beam centers and observational point. Those variations however form an oscillation of the PE maximum around 130 m depth, unlike observations which show NIW-modulation in the form of energy bands observed over several hundreds of meters. We hence believe that the mechanism proposed by Broutman et al. (1986) is the most plausible explanation for the SD modulation at near-inertial frequencies that we observe. Fully non-linear simulations and turbulent dissipation measurements during future field studies will however be needed to ascertain the validity of this hypothesis and to estimate the internal tide dissipation rate associated with this process. It is worth noting that this process is fundamentally different from the direct generation of harmonics at the sum of tidal and inertial frequencies as observed by Davies and Xing (2003), which would not produce a modulation of the internal tide energy at the near inertial period.

The process described above can enhance vertical mixing in the ocean by concentrating the tidal energy and/or decreasing the vertical wavelength such that the flow can become super critical. This process can only affect internal tides when there is a sufficient scale separation between the internal tide and NIWs. The tropical region, where the semi-diurnal frequency is much higher than f, is favorable for this scale-separation. This process also requires a strong high-frequency wind variability that can generate NIWs, as for example in regions where deep atmospheric convection and low-pressure systems frequently form. The dissipation of internal tides by this process will mostly occur in the upper 150m, where most NIW energy is concentrated (Furuichi et al. 2008). Small-scale internal tides are mostly generated near mid-ocean ridges such as the Indian and mid-Atlantic ridges and the East Pacific rise (St. Laurent and Garrett 2002). The intersection of these generation sites with the tropical band represents a large fraction of the global internal tide generation (Egbert and Ray, 2001, Nycander, 2005, Melet et al., 2013). There is hence a potential for this focusing process to be relevant on a global scale, confirmation of which will rely on further observational and modeling work.

Acknowledgements

We would like to thank the crew of R/V *Suroît* and captain T. Alix; and all the scientific and technical crew onboard. R/V *Suroît* is an Ifremer ship. Institut National des Sciences de l'Univers (INSU) provided technical and financial support for the Cirene cruise. Observational data from the Cirene campaign analyzed in this article are available, upon request, to Yannis Cuypers, (Yannis.Cuypers@locean-ipsl.upmc.fr) or Jérôme Vialard (Jerome.Vialard@ird.fr). This is PMEL contribution no. 4434.

References

Broutman, D., & Young, W. R. (1986). On the interaction of small-scale oceanic internal waves with near-inertial waves. *Journal of Fluid Mechanics*, *166*, 341-358.

Broutman, D. (1986). On internal wave caustics. *Journal of physical oceanography*, *16*(10), 1625-1635.

Broutman, D., Macaskill, C., McIntyre, M. E., & Rottman, J. W. (1997). On Doppler□spreading models of internal waves. *Geophysical research letters*,*24*(22), 2813-2816.

Chavanne, C., Flament, P., Carter, G., Merrifield, M., Luther, D., Zaron, E., & Gurgel, K. W. (2010). The Surface Expression of Semidiurnal Internal Tides near a Strong Source at Hawaii. Part I: Observations and Numerical Predictions*. *Journal of Physical Oceanography*, *40*(6), 1155-1179.

Cuypers, Y., Le Vaillant, X., Bouruet-Aubertot, P., Vialard, J., & McPhaden, M. J. (2013). Tropical storm□induced near□inertial internal waves during the Cirene experiment: Energy fluxes and impact on vertical mixing. *Journal of Geophysical Research: Oceans*, *118*(1), 358-380.

Davies, A. M., & Xing, J. (2003). On the interaction between internal tides and wind-induced near-inertial currents at the shelf edge. Journal of Geophysical Research: Oceans, 108(C3).

Egbert, G. D., & Ray, R. D. (2001). Estimates of M2 tidal energy dissipation from TOPEX/Poseidon altimeter data. *Journal of Geophysical Research: Oceans (1978–2012)*, *106*(C10), 22475-22502.

Egbert, G. D., & Erofeeva, S. Y. (2002). Efficient inverse modeling of barotropic ocean tides. *Journal of Atmospheric and Oceanic Technology*, 19(2), 183-204.

Furuichi, N., Hibiya, T., & Niwa, Y. (2008). Model-predicted distribution of wind-induced internal wave energy in the world's oceans. *Journal of Geophysical Research: Oceans*, 113(C9).

Gayen, B., & Sarkar, S. (2013). Degradation of an internal wave beam by parametric subharmonic instability in an upper ocean pycnocline. *Journal of Geophysical Research: Oceans*, 118(9), 4689-4698.

Gerkema, T. (2002). Application of an internal tide generation model to baroclinic spring□neap cycles. *Journal of Geophysical Research: Oceans (1978–2012)*, *107*(C9), 7-1.

Gerkema, T., & van Haren, H. (2012). Absence of internal tidal beams due to non-uniform stratification. *Journal of Sea Research*, *74*, 2-7.

Hayes, W. D. (1970, December). Kinematic wave theory. In *Proceedings of the Royal Society of London A: Mathematical, Physical and Engineering Sciences* (Vol. 320, No. 1541, pp. 209-226). The Royal Society.

Kelly, S. M., & Nash, J. D. (2010). Internal□tide generation and destruction by shoaling internal tides. *Geophysical Research Letters*, *37*(23).

Kelly, S. M., Jones, N. L., Nash, J. D., & Waterhouse, A. F. (2013). The geography of semidiurnal mode-1 internal-tide energy loss. *Geophysical Research Letters*, 40(17), 4689-4693.

Levinson, D. H., H. J. Diamond, K. R. Knapp, M. C. Kruk, and E. J. Gibney, 2010: Toward a homogenous global tropical cyclone best track dataset. *Bull. Am. Met. Soc.,* **91,** 377-380.

Locarnini, R. A., A. V. Mishonov, J. I. Antonov, T. P. Boyer, H. E. Garcia, O. K. Baranova, M. M. Zweng, C. R. Paver, J. R. Reagan, D. R. Johnson, M. Hamilton, and D. Seidov, (2013). *World Ocean Atlas 2013, Volume 1: Temperature.* S. Levitus, Ed., A. Mishonov Technical Ed.; NOAA Atlas NESDIS 73, 40 pp.

Melet, A., Nikurashin, M., Muller, C., Falahat, S., Nycander, J., Timko, P. G., & Goff, J. A. (2013). Internal tide generation by abyssal hills using analytical theory. *Journal of Geophysical Research: Oceans*, *118*(11), 6303-6318.

Nycander, J. (2005). Generation of internal waves in the deep ocean by tides.*Journal of Geophysical Research: Oceans (1978–2012)*, *110*(C10).

Olbers, D. J. (1981). The propagation of internal waves in a geostrophic current. *Journal of physical oceanography*, *11*(9), 1224-1233.

Park, B. C. S., T. W., (1987), Digital Filter Design. John Wiley & Sons.

Ponte, A. L., & Klein, P. (2015). Incoherent signature of internal tides on sea level in idealized numerical simulations. *Geophysical Research Letters*, *42*(5), 1520-1526.

Polzin, K. L., Toole, J. M., Ledwell, J. R., & Schmitt, R. W. (1997). Spatial variability of turbulent mixing in the abyssal ocean. *Science*, *276*(5309), 93-96.

Rainville, L., & Pinkel, R. (2006). Propagation of low-mode internal waves through the ocean. *Journal of Physical Oceanography*, 36(6), 1220-1236.

Smith, W. H., & Sandwell, D. T. (1997). Global sea floor topography from satellite altimetry and ship depth soundings. *Science*, *277*(5334), 1956-1962.

St. Laurent, L. C., & Garrett, C. (2002). The role of internal tides in mixing the deep ocean. *Journal of Physical Oceanography*, *32*(10), 2882-2899.

St. Laurent, L. C., & Nash, J. D. (2004). An examination of the radiative and dissipative properties of deep ocean internal tides. *Deep Sea Research Part II: Topical Studies in Oceanography*, 51(25), 3029-3042.

Sun, O. M., & Pinkel, R. (2013). Subharmonic energy transfer from the semidiurnal internal tide to near-diurnal motions over Kaena Ridge, Hawaii. *Journal of Physical Oceanography*, 43(4), 766-789.

Vanderhoff, J. C., Nomura, K. K., Rottman, J. W., & Macaskill, C. (2008). Doppler spreading of internal gravity waves by an inertia‐wave packet. *Journal of Geophysical Research: Oceans (1978–2012)*, *113*(C5).

Vialard, J., Duvel, J. P., Mcphaden, M. J., Bouruet-Aubertot, P., Ward, B., Key, E., ... & Cassou, C. (2009). CIRENE. *Bulletin of the American Meteorological Society*, 90(1), 45. Whalen, C. B., Talley, L. D., & MacKinnon, J. A. (2012). Spatial and temporal variability of global ocean mixing inferred from Argo profiles. *Geophysical Research Letters*, 39(18).

Wunsch, C., & Ferrari, R. (2004). Vertical mixing, energy, and the general circulation of the oceans. *Annu. Rev. Fluid Mech.*, *36*, 281-314.

Zaron, E. D., & Egbert, G. D. (2014). Time-variable refraction of the internal tide at the Hawaiian Ridge. *Journal of Physical Oceanography*, *44*(2), 538-557.

Zweng, M.M, J.R. Reagan, J.I. Antonov, R.A. Locarnini, A.V. Mishonov, T.P. Boyer, H.E. Garcia, O.K. Baranova, D.R. Johnson, D.Seidov, M.M. Biddle, (2013). *World Ocean Atlas 2013, Volume 2: Salinity*. S. Levitus, Ed., A. Mishonov Technical Ed.; NOAA Atlas NESDIS 74, 39 pp.

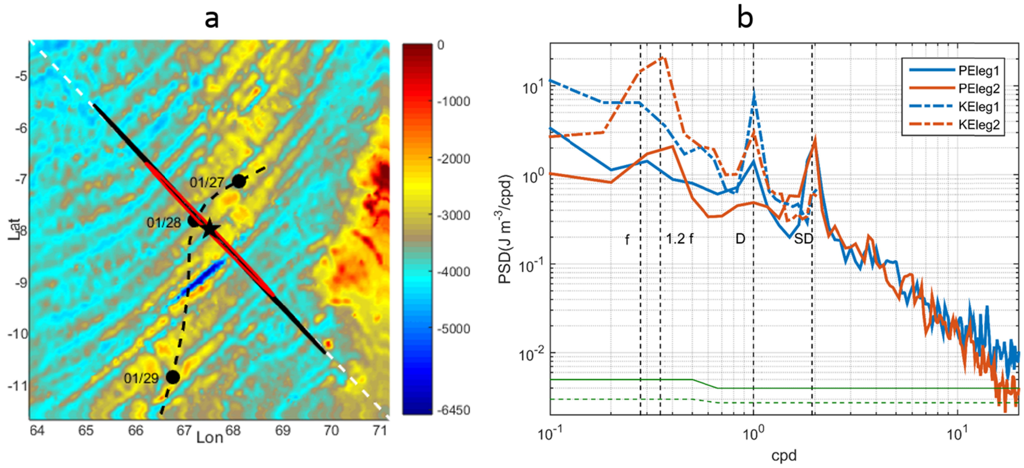

Figure 1 (a) Bathymetry in the Cirene region. The black star indicates the Cirene measurement position (8°S 67.5°E). The black dashed line is the trajectory of cyclone Dora from the IBTraCs database (Levinson et al. 2010). The black and red ellipses respectively represent the M2 and S2 barotropic tidal ellipses, the white dashed line represents the two-dimensional numerical model plane; (b) 0 to 500 m depth averaged spectrum from Cirene observations during leg1 (in blue) and leg2 (in red): Kinetic Energy (KE) as dashed lines, Potential Energy (PE) as solid lines. The vertical black dashed lines indicate the inertial (f), near-inertial (1.2f), tidal Diurnal (D) and Semi-Diurnal (SD) frequencies. The distance between the green dashed line and the green plain line (bottom line) represents the upper (lower) bound of the 95% confidence interval.

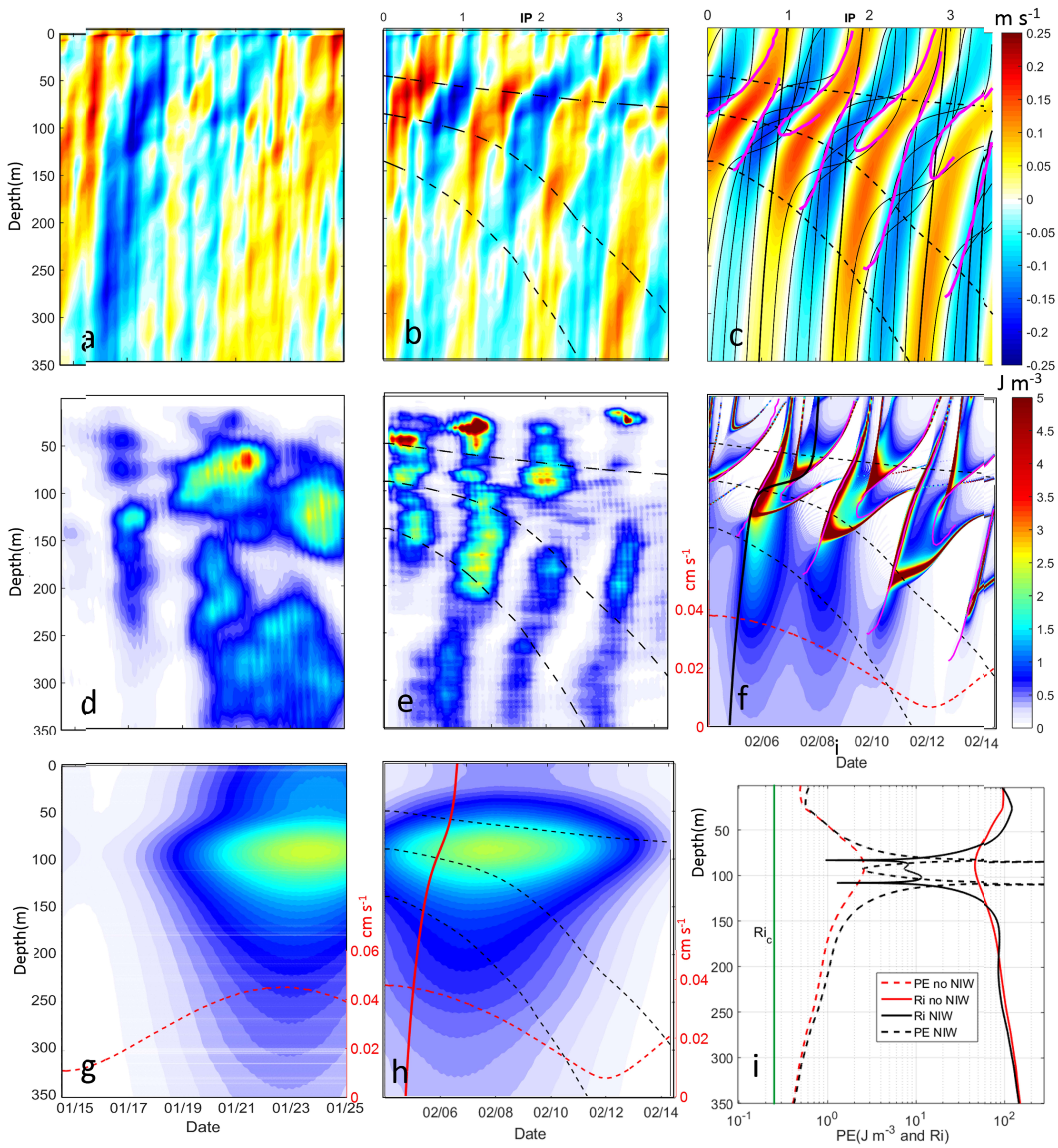

Figure 2 (a) leg1 and (b) leg2 L-ADCP velocities with upward phase propagation projected on the semi-diurnal tidal ellipse axis. (c) Prescribed idealized NIW velocity field for Eikonal equation integrations for leg2. (d) leg1 and (e) leg2 observations of the internal wave Potential Energy PE_{dn} (see text for details). (f), leg2 and (g) leg1 PE along ray trajectories in the Eikonal model, (h) same as (f) when refraction by the NIW shear is not considered. (i) PE (dashed line) and Richardson number Ri (plain line) along the plain red (see panel h) and plain black (see panels f) ray trajectories. The black lines in (c) indicate some internal tide ray trajectories. The black dashed lines in (b), (c), (e), (f), (h) represent the NIW packet envelope. The magenta plain lines in (c) and (f) represent the estimated caustic curves. For panels (b), (c), (e), (f), (h) the upper axis is in near-inertial periods (IP). The red dashed lines at the bottom of panels (f), (g) and (h) represent the SD barotropic tidal envelope of the current amplitude the corresponding scale is on the right (left) of (g),(h) ((f)), .

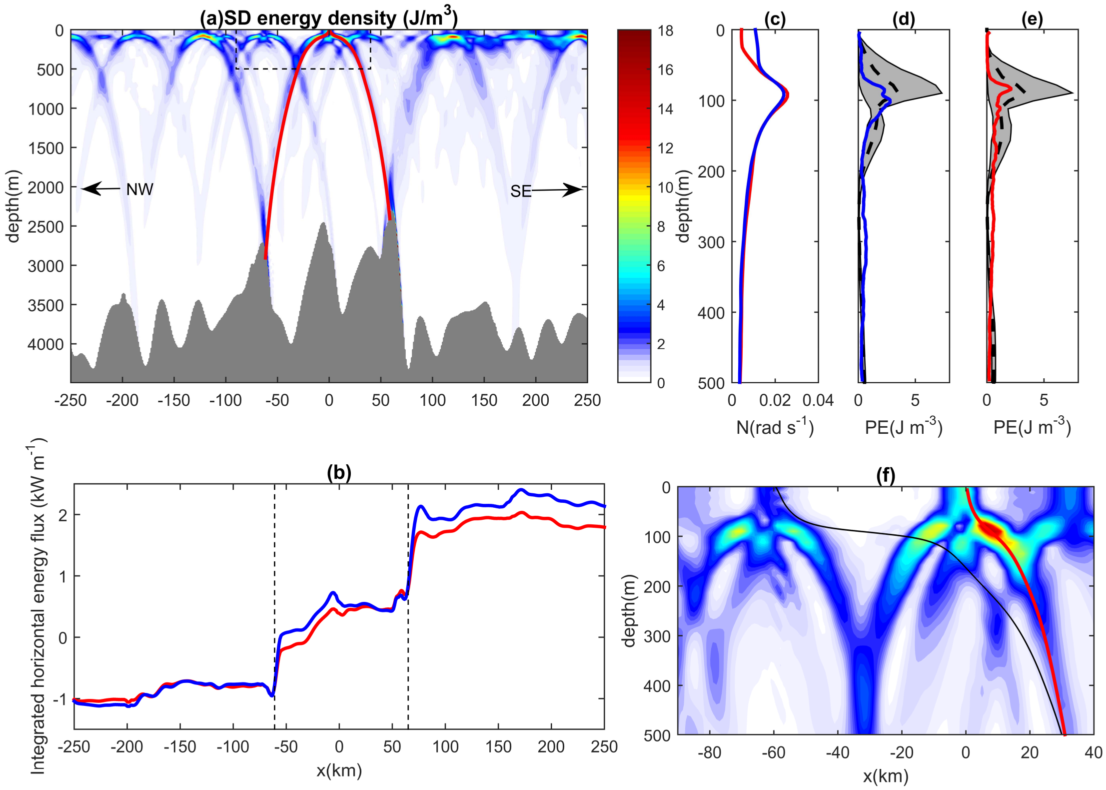

Figure 3 (a) Semi-diurnal tide energy density vertical section along the white dashed line in figure 1a in the numerical model. The red lines indicate internal tide ray trajectory in the absence of background velocity. (b) depth-averaged horizontal energy flux in the numerical model, leg1 in blue, leg2 in red. (c) Mean Brunt Väisälä frequency during leg1 in blue, leg2 in red. (d) leg1 and (e) leg2 mean observed PE density, in red and blue for observations, as a black dashed line for the model average within 3 km of observations with the range of variation in this region indicated as a grey shading. (f) zoom corresponding to the dashed frame on panel (a), with the trajectory of an internal wave ray in the absence of background velocity in red dashed line and when the idealized near-inertial wave velocity field and background current are included in black dashed line. The corresponding trajectories in the (z,t) plane are represented in Fig. 2f and h.